

Helical spin liquid in a triangular XXZ magnet from Chern-Simons theory

Tigran Sedrakyan,^{1,2} Roderich Moessner,² and Alex Kamenev³

¹*Precision Many-Body Physics Initiative, Physics Department, University of Massachusetts, Amherst, Massachusetts 01003, USA*

²*Max-Planck-Institut für Physik komplexer Systeme, Nöthnitzer Straße 38, D-01187 Dresden, Germany*

³*William I. Fine Theoretical Physics Institute, School of Physics and Astronomy, University of Minnesota, Minneapolis, Minnesota 55455, USA*

(Dated: July 23, 2020)

We propose a finite-temperature phase diagram for the 2D spin-1/2 $J_1 - J_2$ XXZ antiferromagnet on the triangular lattice. Our analysis, based on a composite fermion representation, yields several phases. This includes a zero-temperature helical spin liquid with $N = 6$ *anisotropic* Dirac cones, and with nonzero vector chirality implying a broken \mathbb{Z}_2 symmetry. It is terminated at $T = 0$ by a continuous quantum phase transition to 120° ordered state around $J_2/J_1 \approx 0.089$ in the XX limit; these phases share a double degeneracy, which persists to finite T above the helical spin liquid. By contrast, at $J_2/J_1 \approx 0.116$, the transition into a stripe phase appears as first order. We further discuss experimental and numerical consequences of the helical order and the anisotropic nature of the Dirac dispersion.

I. INTRODUCTION

Two-dimensional $s = 1/2$ magnets with frustrated interactions attract a great deal of interest because of their potential to host unconventional states of quantum matter such as spin liquids (SL)¹⁻⁹. Quantum SL are long range entangled states that give rise to emergent gauge fields and represent deconfined phases, where the quasi-particles exhibit fractional quantum numbers. They do not break rotational symmetry, thus excluding orientational long range ordering. Traditionally, the triangular lattice has been regarded as a promising ground for realization of a SL¹⁰⁻¹⁵. In this setting, the frustrated spin-1/2 $J_1 - J_2$ XXZ antiferromagnet on a triangular lattice is one such candidates for a SL ground state in a parameter window around $J_2/J_1 \sim 0.1$. The Hamiltonian of the model is given by

$$\hat{H} = \hat{H}_1 + \hat{H}_2, \text{ where} \quad (1)$$

$$\hat{H}_l = \frac{J_l}{2} \sum_{\mathbf{r}, \nu} [\hat{S}_{\mathbf{r}}^+ \hat{S}_{\mathbf{r}+\boldsymbol{\mu}_\nu}^- + \hat{S}_{\mathbf{r}}^- \hat{S}_{\mathbf{r}+\boldsymbol{\mu}_\nu}^+ + 2g \hat{S}_{\mathbf{r}}^z \hat{S}_{\mathbf{r}+\boldsymbol{\mu}_\nu}^z],$$

where $l = 1, 2$ and a parameter g measures the anisotropy of the interactions. Vectors $\boldsymbol{\mu}_\nu^1 = \mathbf{e}_\nu$ and $\boldsymbol{\mu}_\nu^2 = \mathbf{a}_\nu$, $\nu = 1, 2, 3$, point to nearest neighbor (NN) and next nearest neighbor (NNN) sites on the triangular lattice, respectively. The spin-orbit coupled version of the model is believed to be related to the triangular lattice antiferromagnet YbMgGaO₄¹⁶⁻²¹.

The Heisenberg model, $g = 1$, has been studied numerically using variational Monte-Carlo²²⁻²⁵ and the density matrix renormalization group (DMRG)²⁶⁻²⁹. The DMRG study of Refs. [28,29] and the variational Monte-Carlo study of Ref. [24] explore the phase diagram of the model Eq. (1) ranging from the XX limit, $g = 0$, all the way to the Heisenberg limit with $g = 1$. The nature of the SL in Ref. [24] was identified with the $U(1)$ Dirac gauge theory which emerges in the Heisenberg limit

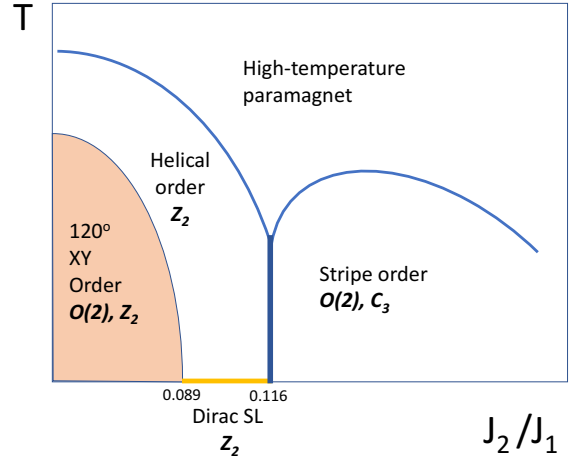


FIG. 1: (Color online) A schematic finite-temperature phase diagram of the $J_1 - J_2$ XXZ model on a triangular lattice from our composite Fermion analysis. Broken symmetries are indicated in bold font. The thick (blue) line represents the first-order transition from helical into stripe ordered phases. Thick horizontal (yellow) line represents the $T = 0$ helical Dirac SL. Numerical values for J_2/J_1 correspond to the XX case, $g = 0$.

in an approximate parameter interval $0.08 \lesssim t \lesssim 0.2$, $t = J_2/J_1$ ^{23,25}. The interval where the SL is realized appears to be narrower in the XXZ model^{24,28,29}.

In this work we carry out an analysis based on a composite Fermion representation. An advantage of the fermion representation is that it can be used to effectively describe both the ordered phases as CS superconductors³⁰, and spin-liquids, where the fermions can be "deconfined." There are two main differences between our work and previous approaches to establish spin-liquids: in our framework, we start by focusing on the ordered states of the spin-1/2 XXZ magnet via treat-

ing it as superconducting states of spinless Chern-Simons fermions. We then study the stability region of the ordered state, assuming the spin-liquid emerges when the ordering breaks down. Apart from developing the general approach based on breaking of the Chern-Simons superconductivity for detecting instability of the spin-order, we apply the method to the specific model under consideration. The purpose of this application is to propose a new state – the helical spin liquid. In part, our work is a study that suggests the existence of new types of phases with peculiar properties, which also indicates where they may be realized. Our approach proposes a novel scenario of unconventional (deconfined) phase transitions and novel quantum phases that can be realized in frustrated magnets.

The performed analysis leads us to propose that the rotational $O(2)$ symmetry is restored, and a kind of Dirac SL is stabilized in the XXZ model in a narrow interval of parameter $t = J_2/J_1$, eg. $0.089 \lesssim t \lesssim 0.116$ in XX limit. The nature of this SL appears to be different from the Heisenberg limit in a crucial way: in the XXZ model it exhibits spontaneous breaking of the \mathbb{Z}_2 symmetry, inherent to the 120° antiferromagnetic ordering of the XX model at $J_2 = 0$. We thus predict a SL with long range \mathbb{Z}_2 order and the *vector chirality* playing the role of the order parameter which distinguishes between two degenerate SL ground states. The other central finding is that such a SL is described in terms of $N = 6$ copies of Dirac fermions. Each Dirac cone is predicted to exhibit a uniaxial anisotropy, although the complete spectrum preserves the C_3 symmetry of the lattice. A finite vector chirality and the anisotropy of individual Dirac cones are the main properties of the proposed SL, dubbed here *Helical SL*, which may be detected using DMRG, tensor network, or variational Monte-Carlo approaches. They may be also observed in spin resolved neutron scattering.

Furthermore, our theory predicts a rich finite-temperature phase diagram, Fig. 1. As in the classical XX model^{31–33}, a BKT transition takes place first into a helical phase with restored $O(2)$, but broken \mathbb{Z}_2 symmetries. At yet higher temperature, there is an Ising-like transition to a disordered paramagnet. Finally, we argue that the $T = 0$ transition from 120° ordered state to the helical SL is continuous, while the one into the stripe phase is first order.

We treat these transitions by first developing a theory of the 120° state via Chern-Simons (CS) superconductivity³⁰, considering the stability of the superconducting solution upon increasing t . The superconducting order breaks down at $t \sim 0.089$ for $g = 0$, signaling an emergence of the Dirac SL state with broken \mathbb{Z}_2 symmetry. Next, we identify a CS superconductor describing the collinear stripe phase, energetically favorable beyond $t \sim 0.116$.

The Hamiltonian (1) can be regarded as a model of hard-core bosons hopping on a triangular lattice with NN amplitude J_1 and NNN amplitude J_2 . At small J_2 (small $t < 1/8$), the single boson dispersion exhibits two

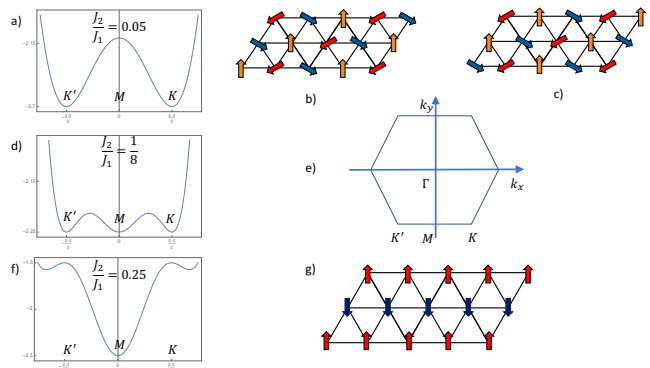


FIG. 2: (Color online) (a), (d), (f): Single particle dispersion relations on a triangular lattice for different values of $t = J_2/J_1$. Schematic nature of the phases condensed at the K' (b), K' (c) and M (g) points of the BZ (e).

degenerate minima located at the K and K' points of the Brillouin zone (BZ), Fig. 2a. This implies that noninteracting bosons can condense to any superposition of these two states, however the hard-core interactions prevent forming a density modulation and enforce condensation into one of these two points. This leads to the doubly degenerate ground states, identified with the planar 120° Néel configurations of spins with two helicities, Figs. 2b,c. At $t = 1/9$ the single particle dispersion acquires an additional minimum at the M point, midway between K and K' , while at $t = 1/8$ the dispersion is triply degenerate, Figs. 2d and 2e. At $t > 1/8$ the global minimum is at M , signaling semiclassically a first order transition^{34,35} into a state with the collinear stripe order shown in Fig. 2g.

II. EMERGENCE OF ANISOTROPIC DIRAC FERMIONS

This picture is severely modified by quantum fluctuations. We account for these by reformulating the model (1) as a theory of *spinless* lattice fermions coupled to a CS gauge field. The fermionization automatically takes care of the hard-core condition. The spin operators may be represented as $S_{\mathbf{r}}^{\pm} = \exp\left(ie \sum_{\mathbf{r}' \neq \mathbf{r}} \arg[\mathbf{r} - \mathbf{r}'] n_{\mathbf{r}'}\right) f_{\mathbf{r}}^{\pm}$, where $e = 2l + 1$ is an odd integer representing the CS charge, $f_{\mathbf{r}}^{\pm}$ are creation/annihilation operators of canonical spinless fermions, $n_{\mathbf{r}} = f_{\mathbf{r}}^{\dagger} f_{\mathbf{r}} = S_{\mathbf{r}}^{+} S_{\mathbf{r}}^{-}$ is the particle number operator, and summation runs over all lattice sites. The XX part of the Hamiltonian (1) acquires the form:

$$H_I = \frac{J_I}{2} \sum_{\mathbf{r}, \nu} f_{\mathbf{r}}^{\dagger} f_{\mathbf{r}+\mu_{\nu}} e^{i\Lambda_{\mathbf{r}, \mathbf{r}+\mu_{\nu}}} + H.c., \quad (2)$$

where $\Lambda_{\mathbf{r}_1, \mathbf{r}_2} = \sum_{\mathbf{r}} [\arg(\mathbf{r}_1 - \mathbf{r}) - \arg(\mathbf{r}_2 - \mathbf{r})] n_{\mathbf{r}}$ is a gauge field associated with the NN and NNN links on the triangular lattice. It introduces CS magnetic flux threading the unit cell of the triangular lattice: $\Phi_{\mathbf{r}} =$

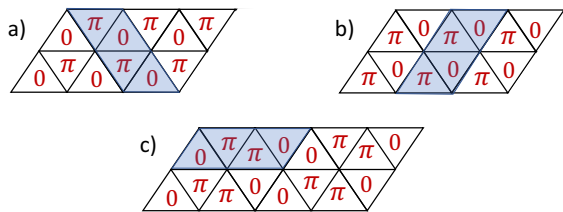


FIG. 3: (Color online) a) and b) Distinct π flux configurations of CS fermionization, corresponding to two helicities of the 120° order. c) π flux configuration corresponding to the stripe order.

$\Lambda_{\mathbf{r},\mathbf{r}+\mathbf{e}_1} + \Lambda_{\mathbf{r}+\mathbf{e}_1,\mathbf{r}+\mathbf{e}_1+\mathbf{e}_2} + \Lambda_{\mathbf{r}+\mathbf{e}_1+\mathbf{e}_2,\mathbf{r}+\mathbf{e}_2} + \Lambda_{\mathbf{r}+\mathbf{e}_2,\mathbf{r}}$, which is the lattice analog of $\Phi_{\mathbf{r}} = \text{curl } \Lambda$ (for details see Appendix A). The Hamiltonian (1) thus can be rewritten in terms of fermions^{30,36-40}, $f_{\mathbf{r}}$, coupled to the $U(1)$ CS gauge field³⁷.

To illustrate how this $U(1)$ field affects the fermion dynamics, we analyze the XX limit of the Hamiltonian (1). In the absence of a net magnetization the CS fermion state is half-filled, $\langle n \rangle = 1/2$. This implies that the CS phases create $2i\pi\langle n \rangle \rightarrow i\pi$ flux, threading the unit cell. The double degeneracy (two helicities) of the 120° state is reflected in the staggered π flux patterns, Figs. 3a,b, for which there are two inequivalent choices, distinguished by the sign of the z -component of the *vector chirality*, defined on a triangular plaquette as^{41,42}

$$\kappa_z = \epsilon_{ij} \left(\langle \hat{S}_1^i \hat{S}_2^j \rangle + \langle \hat{S}_2^i \hat{S}_3^j \rangle + \langle \hat{S}_3^i \hat{S}_1^j \rangle \right), \quad (3)$$

where $\langle \dots \rangle$ stands for the quantum expectation value and $i, j = x, y$. Importantly, this \mathbb{Z}_2 order parameter, reflecting the two different π flux patterns, persists in the SL phase, again implying a double degeneracy.

Consider now the fermionized Hamiltonian for $J_2 > 0$. The NNN bonds form three disjoint large triangular lattices, labelled as $\tau = 1, 2, 3$. At half-filling, fermions hopping along these bonds still accumulate a π flux through a large rhomboidal cell composed of NNN links. The CS transformation unambiguously identifies the π -flux configuration depicted in Fig. 4a for one of the three sublattices, $\tau = 1$. Flux patterns of the two other NNN sublattices are obtained by rotation of Fig. 4a by $\pm 2\pi/3$. Such an arrangement of π fluxes on three NNN triangular lattices preserves C_3 symmetry. However, it further violates the translational invariance in three lattice spacings and, thus the unit cell becomes 6 times larger than the original one. Correspondingly, there is a 6 component Fermi field, $f_{\mathbf{k},\alpha}^\tau$, where $\alpha = 1, 2$ and $\tau = 1, 2, 3$, in a 6 times reduced BZ, leading to a 6×6 Hamiltonian (for details see Appendix B).

The corresponding band structure exhibits two Dirac points, P and \bar{P} , in the reduced BZ, Fig 4b. The momentum space Hamiltonian expanded near the Dirac points

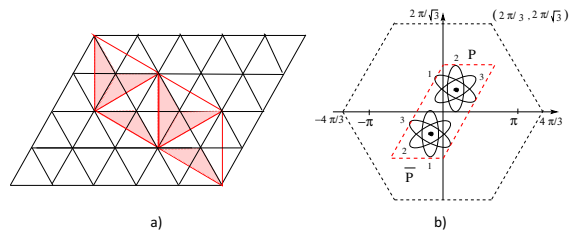


FIG. 4: a) π flux configuration on the NNN large triangular sub-lattice, $\tau = 1$. Each shaded 120° triangle is threaded by π flux. b) Reduced BZ (red), $1/6^{\text{th}}$ of the original BZ (black), with Dirac points P and \bar{P} . The ellipses indicate anisotropic dispersion relations of Dirac fermions labeled by $\tau = 1, 2, 3$.

is $\mathcal{H}^L = H_0^{(P)} + H_0^{(\bar{P})} + H_{int}$, where

$$H_0^{(P)}(\mathbf{k}) = v \sum_{\mathbf{k},\nu,\tau} \hat{f}_{\mathbf{k},\alpha}^{\tau\dagger} [(p_\nu + tq_\nu)\sigma_{\alpha\nu}^\nu - 2tq_\tau\sigma_{\alpha\beta}^\tau] \hat{f}_{\mathbf{k},\beta}^\tau, \quad (4)$$

and its time-reversed partners $H_0^{(\bar{P}\tau)}(\mathbf{k}) = [H_0^{(P\tau)}(-\mathbf{k})]^*$

with $\hat{f}_{\mathbf{k},\alpha}^\tau \rightarrow \hat{f}_{\mathbf{k},\alpha}^{\tau\dagger}$, and $v = J_1 a$, a being the lattice constant. We use: $p_\nu = \mathbf{k} \cdot \mathbf{e}_\nu$ and $q_\nu = \mathbf{k} \cdot \mathbf{a}_\nu$, $\nu = 1, 2, 3$. Hereafter we work with dimensionless quantities measuring energy in units of J_1 and momentum in units of $1/a$. The low-energy fermion operators, $\hat{f}_{\mathbf{k},\alpha}^\tau$ and $\hat{f}_{\mathbf{k},\alpha}^{\tau\dagger}$ have momenta measured from P and \bar{P} points, respectively. The C_3 invariance is ensured by $2\pi/3$ rotations of the lattice accompanied with cyclic transformation, $\tau \rightarrow \tau + 1$, of the fermion copy. The Hamiltonian (4) leads to the *anisotropic* spectrum

$$E_{0,\mathbf{k}}^\tau = \pm \left[(1 + 3t^2) \sum_{\nu=1}^3 p_\nu^2 - 4tp_\tau q_\tau \right]^{1/2}. \quad (5)$$

The 120° state with the other helicity corresponds to $\mathcal{H}^R = H_0^{(P')} + H_0^{(\bar{P}')} + H_{int}$. Note that the ground state spontaneously chooses one of the two.

Upon a gauge transformation, the CS phases in Eq. (2) may be rewritten as covariant derivatives, leading to the substitution $\mathbf{k} \rightarrow \mathbf{k} - e\mathbf{A}_{\mathbf{r}}$ in Eq. (4). Here $\mathbf{A}_{\mathbf{r}}$ in the kinetic term reflects fluctuations of the CS phases from 0 or π per plaquette and is bilinear in fermion operators. It thus generates a two particle interaction vertex^{30,36}

$$H_{int} = - \sum_{\mathbf{k},\mathbf{k}',\mathbf{q},\tau} V_{\mathbf{q}}^{\alpha\alpha',\beta\beta'} \hat{f}_{\mathbf{k},\alpha}^{\tau\dagger} \hat{f}_{\mathbf{k}+\mathbf{q},\alpha'}^\tau \hat{f}_{\mathbf{k}',\beta}^\tau \hat{f}_{\mathbf{k}+\mathbf{q},\beta'}^\tau, \quad (6)$$

where $V_{\mathbf{q}}^{\alpha\alpha',\beta\beta'} = 2\pi i e \left(\sigma_{\alpha\beta}^\nu \delta_{\alpha'\beta'} + \delta_{\alpha\beta} [\sigma_{\alpha'\beta'}^\nu]^T \right) B_{\mathbf{k}}^\nu$ where $\nu = 1, 2, 3$ and $B_{\mathbf{k}}^\nu = \epsilon_{ij} A_{\mathbf{k}}^j (e_\nu^i + ta_\nu^i)$ is determined by the Fourier image $\mathbf{A}_{\mathbf{k}} = \mathbf{k}/|\mathbf{k}|^2$ of the vector potential of the vortex gauge field $\mathbf{A}_{\mathbf{r}}$ defined above.

III. CHERN-SIMONS SUPERCONDUCTIVITY: DESCRIPTION OF PHASES AND DECONFINED PHASE TRANSITION

In this section, we will discuss the Chern-Simons superconductor description of ordered phases, the emergence of the Helical spin-liquid, and the deconfined phase transition from 120° state to the Helical spin-liquid.

A. Chern-Simons superconductor description of the 120° state

The CS interaction (6) leads to the Cooper pairing of fermions residing near the P and \bar{P} points and may result in a broken $U(1)$ superconducting phase. In terms of the original spins the latter corresponds to a broken $O(2)$ 120° antiferromagnet. Upon increasing t , the fermion dispersion becomes more anisotropic, weakening the Cooper pairing (which operates only within time-reversal pairs with the same NNN sub-lattice index τ , Eq. (6), which has a non-collinear anisotropy orientation in P and \bar{P} points, Fig. 4b). This leads to an eventual breakdown of the CS superconductivity at $t \approx 0.089$.

To describe this physics we employ the standard BCS treatment with the superconducting order parameter $\Delta_{\mathbf{k}}^{\alpha\alpha'} = -2\pi ie \sum_{\beta\beta'\mathbf{k}'} V_{\mathbf{k}-\mathbf{k}'}^{\alpha\alpha',\beta\beta'} \langle \hat{f}_{-\mathbf{k}',\beta} \hat{f}_{\mathbf{k}',\beta'} \rangle$, where the index τ is dropped hereafter. The order parameter is quadratically coupled to the fermions as: $\sum_{\alpha\alpha'\mathbf{k}} \Delta_{\mathbf{k}}^{\alpha\alpha'} \hat{f}_{\mathbf{k},\alpha}^\dagger \hat{f}_{-\mathbf{k},\alpha'}^\dagger + H.c.$, leading to self-consistency conditions. Following Ref. [30], one expects $p \pm ip$ symmetry of $\Delta_{\mathbf{k}}^{\alpha\alpha'}$ and thus looks for the solution in the form

$$\Delta_{\mathbf{k}}^{\alpha\alpha'} = \Delta_{3\mathbf{k}} \delta_{\alpha\alpha'} + i \frac{\Delta_{0,\mathbf{k}}}{\sqrt{3}} \sum_{\mu,\nu=1,2,3} \eta_{\mu\nu} (q_\mu - 3tp_\mu) \sigma_{\alpha\alpha'}^\nu, \quad (7)$$

where $\eta_{\mu\nu}$ is defined as $\eta_{33} = 1, \eta_{ij} = \epsilon_{ij}, \eta_{3i} = 0, i, j = 1, 2$. The corresponding self-consistency equations in terms of the scalar order parameters $\Delta_{0,\mathbf{k}}$ and $\Delta_{3,\mathbf{k}}$ are given in Appendix C. At $t = 0$ they exhibit a non-trivial solution³⁰ for CS charge $e = 3$. For $t > 0$ the anisotropy of the Dirac spectrum (5), Fig. 4b, suppresses the order parameter. Fig. 5a shows the corresponding gap in the fermionic spectrum, Δ_{120° , obtained through a numerical solution of the self-consistency equations. The gap and the $U(1)$ broken state collapse at $t = 0.089$, indicating the absence of the planar long range order at larger t . Notice that the \mathbb{Z}_2 symmetry breaking, associated with the choice of CS flux pattern, Fig. 3a,b, remains intact across this transition.

B. Helical spin-liquid phase

For $t > 0.089$, in the CS superconductivity associated with one of the two 120° states, one is left thus with a gapless state with an unbroken $U(1)$ symmetry and excitations described in terms of $N = 6$ copies of Dirac

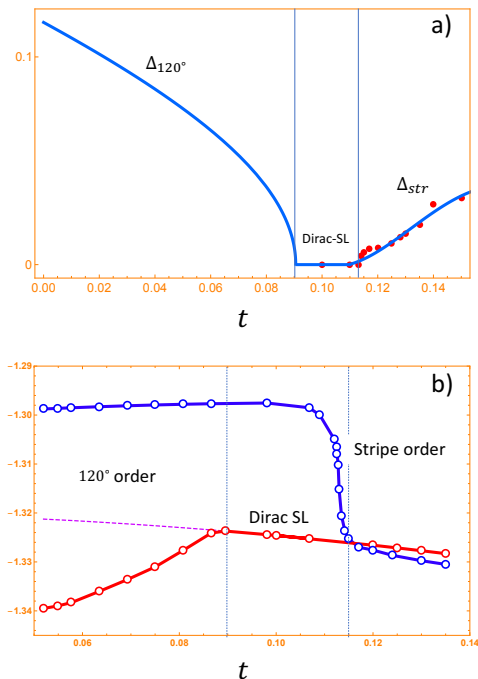


FIG. 5: (Color online) (a) Excitation gap of the fermion spectrum plotted versus $t = J_2/J_1$ in the CS superconductor mean-field description of the 120° state, Dirac SL, and the CS superconductor mean-field description of the striped phase. The superconducting order parameters are zero at $0.089 \lesssim t \lesssim 0.113$. Note that the order parameter Δ_{120° vanishes continuously near $t \sim 0.089$, signaling a continuous phase transition to the SL phase. (b) Ground state energy of gapless Dirac fermions on a triangular lattice at half-filling with π -flux distribution corresponding to Fig. (2a) and/or (2b) as a function of t compared with the energy of the CS superconductor of the striped phase. Note a first order transition at the level crossing near $t \sim 0.116$.

fermions with the anisotropic dispersion. This is the SL ground state, doubly degenerate due to the presence of the the long-range \mathbb{Z}_2 order. The latter may be detected by a finite value of the vector chirality, Eq. (3). To derive an effective low-energy field theory in this regime one should integrate out fermionic degrees of freedom with momenta away from the two Dirac points. This way one obtains a stable⁴³ 2+1 dimensional Maxwell electrodynamics coupled to $N = 6$ copies of the anisotropic Dirac fermions (see Appendix D).

An external magnetic field in the z direction, $H_h = h \sum_{\mathbf{r}} S_{\mathbf{r}}^z$, leads to a deviation from half filling and thus to a non-zero chemical potential of the Dirac fermions. Each additional fermion comes with an extra flux quantum of the gauge field. It results in Landau quantization of the fermionic energies with the fully filled levels. Thus the excitation spectrum of the SL in a magnetic field is *gapped* with the gap proportional to $|h|$.

C. Chern-Simons superconductor description of the stripe phase

Consider an alternative choice of CS flux pattern, depicted in Fig. 3c. This choice breaks the C_3 symmetry and selects a preferred direction along the lattice. The reduced BZ can be chosen to be the same as in Fig. 4b, but the Dirac points are $Q^\pm = (\pm \arccos(t), 0)$. The superconducting solution (see Appendix C) exists for $t \gtrsim 0.113$. However its energy is smaller than that of SL only at $t \gtrsim 0.116$, Fig. 5b, suggesting a first order transition. The corresponding U(1) broken state is the stripe phase, Fig. 2g, which also breaks C_3 lattice symmetry. As a result, the helical SL state appears stabilized in the narrow interval $0.089 \lesssim t \lesssim 0.116$.

IV. DISCUSSION AND ESTIMATES

There are two main differences between our work and previous approaches to establish spin-liquids: in our framework, we start by focusing on the ordered states of the spin-1/2 XXZ magnet via treating it as superconducting states of spinless CS fermions. This approach is as good as other methods (e.g., using Schwinger or Holstein-Primakoff representations of spins) to describe the symmetry broken state. We then study the stability region of the ordered state, taking into account that in the spin-liquid phase the ordering breaks down. Thus, the SL emerges in the parameter window where such superconducting states cannot be established. It would

be desirable to test these predictions with, say, DMRG simulations, although the large number of Dirac points involved may make this technically challenging.

We have mostly focused on the XX case, $g = 0$, while a finite g leads to an additional fermionic interaction vertex, which modifies the self-consistency equations. This leads in turn to a weak g -dependence of the critical values of t . Since the model does not have SU(2) symmetry, the low-energy fermion excitations may be considered spinless, and as such, the SL is outside the projective symmetry group classification of SL's based on Schwinger boson and Abrikosov fermion representation of spins^{14,44,45}. We encourage neutron scattering experiments for observation of the proposed spin liquid state. Here the spin magnetization distribution and spin-spin correlators are expected not to exhibit Bragg peaks. Moreover, the anisotropy of the dynamical structure factor near Dirac points may serve as a signal of the anisotropic Dirac dispersion. The information about the vector chiral order of the spin-liquid may be revealed in nuclear-magnetic interferences in the chiral magnetic scattering⁴⁶⁻⁴⁸ of an initially unpolarized neutron beam.

Acknowledgement

We are indebted to L. Balents, A. Chernyshev, A. Chubukov, O. Starykh and Mengxing Ye for valuable discussions. A.K. was supported by NSF grant DMR-1608238. T.A.S. acknowledges startup funds from UMass Amherst and thanks the Max Planck Institute for the Physics of Complex Systems for hospitality.

Appendix A: Flux configuration for Chern-Simons fermions on the triangular lattice

The Chern-Simons (CS) transformation

$$S_{\mathbf{r}}^\pm = \exp \left(ie \sum_{\mathbf{r}' \neq \mathbf{r}} \arg[\mathbf{r} - \mathbf{r}'] n_{\mathbf{r}'} \right) f_{\mathbf{r}}^\pm, \quad (\text{A1})$$

where the summation is performed over all lattice sites except r , defines the distribution of position-dependent phases on links of the lattice (see Eq. (2) of the main text for definitions). The phase corresponding to the link between sites positioned at \mathbf{r}_1 and \mathbf{r}_2 can be divided into two parts:

$$\Lambda_{\mathbf{r}_1, \mathbf{r}_2} = \sum_{\mathbf{r}' \neq \mathbf{r}_1} \arg[\mathbf{r}_1 - \mathbf{r}'] n_{\mathbf{r}'} - \sum_{\mathbf{r}' \neq \mathbf{r}_2} \arg[\mathbf{r}_2 - \mathbf{r}'] n_{\mathbf{r}'} = \Lambda_{\mathbf{r}_1, \mathbf{r}_2}^\Gamma + \Lambda_{\mathbf{r}_1, \mathbf{r}_2}^L. \quad (\text{A2})$$

The first term, $\Lambda_{\mathbf{r}_1, \mathbf{r}_2}^\Gamma$, is the "global" phase formed from all points \mathbf{r} away from the link $(\mathbf{r}_1, \mathbf{r}_2)$,

$$\Lambda_{\mathbf{r}_1, \mathbf{r}_2}^\Gamma = \sum_{\mathbf{r}' \neq \mathbf{r}_1, \mathbf{r}_2} \left[\arg[\mathbf{r}_1 - \mathbf{r}'] - \arg[\mathbf{r}_2 - \mathbf{r}'] \right] n_{\mathbf{r}'}, \quad (\text{A3})$$

accounting for the scanning angles on the lattice outside of the link $\mathbf{r}_1, \mathbf{r}_2$. The second term, $\Lambda_{\mathbf{r}_1, \mathbf{r}_2}^L$, is the "local" phase formed from the end points of links

$$\Lambda_{\mathbf{r}_1, \mathbf{r}_2}^L = \arg(\mathbf{r}_2 - \mathbf{r}_1) n_{\mathbf{r}_1} - \arg(\mathbf{r}_1 - \mathbf{r}_2) n_{\mathbf{r}_2}. \quad (\text{A4})$$

Now we consider the unit cell rectangle presented in Fig.6(left panel) and calculate the phase acquired by a fermion upon clockwise rotation around it (this is a convention we use). First, we calculate the net phase accumulated from

local phases $\Lambda_{\mathbf{r}_i, \mathbf{r}_j}^L$, coming from the endpoints of the links. According to this expression, one can find the following phases on links depicted in Fig.6(left panel):

$$\begin{aligned}\Lambda_{\mathbf{r}-\mathbf{e}_1, \mathbf{r}-\mathbf{e}_1+\mathbf{e}_2}^L &= \pi n_{\mathbf{r}-\mathbf{e}_1+\mathbf{e}_2}, & \Lambda_{\mathbf{r}-\mathbf{e}_1+\mathbf{e}_2, \mathbf{r}+\mathbf{e}_2}^L &= -\frac{\pi}{3} n_{\mathbf{r}-\mathbf{e}_1+\mathbf{e}_2} + \frac{4\pi}{3} n_{\mathbf{r}+\mathbf{e}_2}, & \Lambda_{\mathbf{r}+\mathbf{e}_2, \mathbf{r}}^L &= -\pi n_{\mathbf{r}+\mathbf{e}_2}, \\ \Lambda_{\mathbf{r}, \mathbf{r}-\mathbf{e}_1}^L &= \frac{\pi}{3} n_{\mathbf{r}-\mathbf{e}_1} - \frac{4\pi}{3} n_{\mathbf{r}}, & \Lambda_{\mathbf{r}-\mathbf{e}_1+\mathbf{e}_2, \mathbf{r}}^L &= -\frac{2\pi}{3} n_{\mathbf{r}-\mathbf{e}_1+\mathbf{e}_2} + \frac{5\pi}{3} n_{\mathbf{r}}\end{aligned}\quad (\text{A5})$$

Here the convention for arg functions is adopted and they are calculated with respect to the x -axes in a counterclockwise direction. The accumulated local fluxes over triangles in the unit cell will be

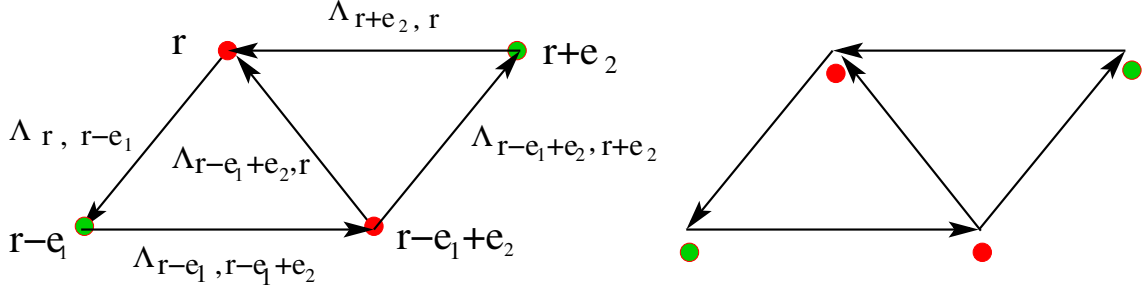


FIG. 6: (Color online) Left panel: A unit cell of the triangular lattice. Phases associated with the links are shown. Right panel: The unit cell is "remedied" with an infinitesimal shift showing that the cell includes one site.

$$\begin{aligned}\Phi_{\mathbf{r}-\mathbf{e}_1, \mathbf{r}-\mathbf{e}_1+\mathbf{e}_2, \mathbf{r}}^L &= \Lambda_{\mathbf{r}-\mathbf{e}_1, \mathbf{r}-\mathbf{e}_1+\mathbf{e}_2}^L + \Lambda_{\mathbf{r}-\mathbf{e}_1+\mathbf{e}_2, \mathbf{r}}^L + \Lambda_{\mathbf{r}, \mathbf{r}-\mathbf{e}_1}^L = \frac{\pi}{3} (n_{\mathbf{r}-\mathbf{e}_1} + n_{\mathbf{r}-\mathbf{e}_1+\mathbf{e}_2} + n_{\mathbf{r}}), \\ \Phi_{\mathbf{r}-\mathbf{e}_1+\mathbf{e}_2, \mathbf{r}+\mathbf{e}_2, \mathbf{r}}^L &= \Lambda_{\mathbf{r}-\mathbf{e}_1+\mathbf{e}_2, \mathbf{r}+\mathbf{e}_2}^L + \Lambda_{\mathbf{r}+\mathbf{e}_2, \mathbf{r}}^L + \Lambda_{\mathbf{r}, \mathbf{r}-\mathbf{e}_1+\mathbf{e}_2}^L = \frac{\pi}{3} (n_{\mathbf{r}-\mathbf{e}_1+\mathbf{e}_2} + n_{\mathbf{r}+\mathbf{e}_2} + n_{\mathbf{r}}) - 2\pi n_{\mathbf{r}}.\end{aligned}\quad (\text{A6})$$

The local flux corresponding to the unit cell will thus be:

$$\Phi_{\mathbf{r}, \mathbf{r}+\mathbf{e}_1, \mathbf{r}+\mathbf{e}_1+\mathbf{e}_2, \mathbf{r}+\mathbf{e}_2}^L = \frac{\pi}{3} (n_{\mathbf{r}-\mathbf{e}_1} + n_{\mathbf{r}+\mathbf{e}_2} + 2n_{\mathbf{r}} + 2n_{\mathbf{r}-\mathbf{e}_1+\mathbf{e}_2}) - 2\pi n_{\mathbf{r}}. \quad (\text{A7})$$

The calculation of global fluxes through triangles is much simpler. The phase on a given link in a triangle is equal to the opposite to the link angle times the density operator corresponding to that site. It is straightforward to obtain

$$\begin{aligned}\Phi_{\mathbf{r}-\mathbf{e}_1, \mathbf{r}-\mathbf{e}_1+\mathbf{e}_2, \mathbf{r}}^\Gamma &= \Lambda_{\mathbf{r}-\mathbf{e}_1, \mathbf{r}-\mathbf{e}_1+\mathbf{e}_2}^\Gamma + \Lambda_{\mathbf{r}-\mathbf{e}_1+\mathbf{e}_2, \mathbf{r}}^\Gamma + \Lambda_{\mathbf{r}, \mathbf{r}-\mathbf{e}_1}^\Gamma = \frac{\pi}{3} (n_{\mathbf{r}-\mathbf{e}_1} + n_{\mathbf{r}-\mathbf{e}_1+\mathbf{e}_2} + n_{\mathbf{r}}), \\ \Phi_{\mathbf{r}-\mathbf{e}_1+\mathbf{e}_2, \mathbf{r}+\mathbf{e}_2, \mathbf{r}}^\Gamma &= \Lambda_{\mathbf{r}-\mathbf{e}_1+\mathbf{e}_2, \mathbf{r}+\mathbf{e}_2}^\Gamma + \Lambda_{\mathbf{r}+\mathbf{e}_2, \mathbf{r}}^\Gamma + \Lambda_{\mathbf{r}, \mathbf{r}-\mathbf{e}_1+\mathbf{e}_2}^\Gamma = \frac{\pi}{3} (n_{\mathbf{r}-\mathbf{e}_1+\mathbf{e}_2} + n_{\mathbf{r}+\mathbf{e}_2} + n_{\mathbf{r}}).\end{aligned}\quad (\text{A8})$$

The global flux through the rectangular unit cell will be

$$\Phi_{\mathbf{r}, \mathbf{r}+\mathbf{e}_1, \mathbf{r}+\mathbf{e}_1+\mathbf{e}_2, \mathbf{r}+\mathbf{e}_2}^\Gamma = \frac{\pi}{3} (n_{\mathbf{r}-\mathbf{e}_1} + n_{\mathbf{r}+\mathbf{e}_2} + 2n_{\mathbf{r}} + 2n_{\mathbf{r}-\mathbf{e}_1+\mathbf{e}_2}). \quad (\text{A9})$$

Finally, one can make use of the obtained expressions to calculate the the total flux threading each of the triangles of the unite cell and the total flux through the the rectangular unit cell itself. Putting all together we see that

$$\begin{aligned}\Phi_{\mathbf{r}-\mathbf{e}_1, \mathbf{r}-\mathbf{e}_1+\mathbf{e}_2, \mathbf{r}} &= \Phi_{\mathbf{r}-\mathbf{e}_1, \mathbf{r}-\mathbf{e}_1+\mathbf{e}_2, \mathbf{r}}^\Gamma + \Phi_{\mathbf{r}-\mathbf{e}_1, \mathbf{r}-\mathbf{e}_1+\mathbf{e}_2, \mathbf{r}}^L \\ &= \frac{2\pi}{3} (n_{\mathbf{r}-\mathbf{e}_1} + n_{\mathbf{r}-\mathbf{e}_1+\mathbf{e}_2} + n_{\mathbf{r}}),\end{aligned}\quad (\text{A10})$$

$$\begin{aligned}\Phi_{\mathbf{r}-\mathbf{e}_1+\mathbf{e}_2, \mathbf{r}+\mathbf{e}_2, \mathbf{r}} &= \Phi_{\mathbf{r}-\mathbf{e}_1+\mathbf{e}_2, \mathbf{r}+\mathbf{e}_2, \mathbf{r}}^\Gamma + \Phi_{\mathbf{r}-\mathbf{e}_1+\mathbf{e}_2, \mathbf{r}+\mathbf{e}_2, \mathbf{r}}^L \\ &= \frac{2\pi}{3} (n_{\mathbf{r}-\mathbf{e}_1+\mathbf{e}_2} + n_{\mathbf{r}+\mathbf{e}_2} + n_{\mathbf{r}}) - 2\pi n_{\mathbf{r}},\end{aligned}\quad (\text{A11})$$

$$\begin{aligned}\Phi_{\mathbf{r}, \mathbf{r}+\mathbf{e}_1, \mathbf{r}+\mathbf{e}_1+\mathbf{e}_2, \mathbf{r}+\mathbf{e}_2} &= \Phi_{\mathbf{r}, \mathbf{r}+\mathbf{e}_1, \mathbf{r}+\mathbf{e}_1+\mathbf{e}_2, \mathbf{r}+\mathbf{e}_2}^\Gamma + \Phi_{\mathbf{r}, \mathbf{r}+\mathbf{e}_1, \mathbf{r}+\mathbf{e}_1+\mathbf{e}_2, \mathbf{r}+\mathbf{e}_2}^L \\ &= \frac{2\pi}{3} (n_{\mathbf{r}-\mathbf{e}_1} + n_{\mathbf{r}+\mathbf{e}_2} + 2n_{\mathbf{r}} + 2n_{\mathbf{r}-\mathbf{e}_1+\mathbf{e}_2}) - 2\pi n_{\mathbf{r}}.\end{aligned}\quad (\text{A12})$$

Here we see that the uniform density smearing approximation, $n_{\mathbf{r}} \rightarrow n = \text{const}$ (n being the lattice filling fraction), still implies that fluxes threading the triangles of the unit cell are not uniform but are modulated: The flux through one of the regular triangles in the unit cell is vanishing while the flux threading the other regular triangle becomes $\Phi \rightarrow 2\pi n$. Such a flux modulation can be qualitatively understood as follows. Fig. 6(right panel) depicts the unit cell, which is shown with an infinitesimally small shift of the sites. Depending on the direction of the shift, the site corresponding to the unit cell is located within one of the two regular triangles. Hence the net flux $2\pi n$ is threading only one of the two regular triangles. At half filling $n = 1/2$ and thus one obtains a π -flux lattice, as shown in Fig.3 of the main text.

Appendix B: Hamiltonian

The CS transformation³⁷ implies a staggered π flux distribution within the NN and NNN triangular sub-lattices. The flux distribution in the NNN triangular sublattices with $\tau = 2, 3$ is obtained from the lattice corresponding to $\tau = 1$ upon rotation by $\pm 2\pi/3$, respectively. Such a phase distribution breaks translational invariance on three lattice steps reducing the Brillouin zone of the NN triangular lattice 6 times.

As a result of the staggered π -flux threading of every other triangle in the unit cell (including both triangles composed on NN and NNN bonds), the single-fermion dispersion on a triangular lattice will acquire a Dirac form around the following points of the first Brillouin zone: $P_\tau = (\pi/6 + 2\pi\tau/3, \pi/2\sqrt{3})$ and $\bar{P}_\tau = (-\pi/6 + 2\pi\tau/3, \pi/2\sqrt{3})$, $\tau = 1, 2, 3$, giving rise to six components of the Fermi field. These Dirac points form a triangular lattice in momentum space (see Fig. 4b of the main text), while the reduced BZ is a rhombus that includes only one pair of points (P_τ, \bar{P}_τ) .

The double degeneracy of the planar 120° state is linked to the interchange of fluxes $\pi \leftrightarrow 0$ threading each triangular face of the unit cell. We note that the chiralities of the Hamiltonian expanded around P_τ and \bar{P}_τ are opposite. Similarly, if one identifies the reflection of P_τ and \bar{P}_τ with respect to the k_x -axis with P'_τ and \bar{P}'_τ , then the chiralities of the corresponding Hamiltonians (expanded around P'_τ and \bar{P}'_τ) will also be opposite to each other. This implies that the single particle states at $t \rightarrow 0$, in close vicinities of these Dirac points, are given by $\bar{u}'_\tau(\mathbf{k}) = u_\tau(\mathbf{k}) = \frac{1}{\sqrt{2}} \begin{pmatrix} e^{-i \arg \mathbf{k}} \\ 1 \end{pmatrix}$,

and $u'_\tau(\mathbf{k}) = \bar{u}_\tau(\mathbf{k}) = [u_\tau(\mathbf{k})]^*$. These states define Berry connections⁴⁹, as $\vec{\mathcal{A}}_\tau = \vec{\mathcal{A}}'_\tau = -i[u_\tau(\mathbf{k})]^\dagger \vec{\partial}_k u_\tau(\mathbf{k})$, $\vec{\mathcal{A}}'_\tau = \vec{\mathcal{A}}_\tau = -i[\bar{u}_\tau(\mathbf{k})]^\dagger \vec{\partial}_k \bar{u}_\tau(\mathbf{k})$, and the Berry phases defined by contours C_τ , $\tau = 1, 2, 3$ encircling both, P_τ and P'_τ points, as $\gamma_\tau = \int_{C_\tau} d\mathbf{k} \vec{\mathcal{A}}_\tau$, and $\gamma'_\tau = \int_{C_\tau} d\mathbf{k} \vec{\mathcal{A}}'_\tau$. The result of integration around each of these Dirac points yields $\gamma_\tau = \bar{\gamma}'_\tau = -\bar{\gamma}_\tau = -\gamma'_\tau = \pi$.

The corresponding Hamiltonian has the form

$$H = \frac{1}{2} \begin{pmatrix} 2t \cos q_1 & 2t(\cos q_2 + i \sin q_3) & e^{ip_1} & e^{ip_2} - e^{ip_3} & e^{-ip_1} & e^{-ip_2} + e^{-ip_3} \\ 2t(\cos q_2 - i \sin q_3) & -2t \cos q_1 & e^{ip_2} + e^{ip_3} & -e^{ip_1} & e^{-ip_2} - e^{-ip_3} & -e^{-ip_1} \\ e^{-ip_2} + e^{-ip_3} & e^{-ip_2} + e^{-ip_3} & -2t \cos q_1 & 2t(-\cos q_2 + i \sin q_3) & e^{ip_1} & e^{ip_2} - e^{ip_3} \\ e^{ip_1} & -e^{-ip_1} & -2t(\cos q_2 + i \sin q_3) & 2J_2 \cos q_1 & e^{ip_2} + e^{ip_3} & -e^{ip_1} \\ e^{ip_2} + e^{ip_3} & e^{ip_2} - e^{ip_3} & e^{-ip_1} & e^{-ip_2} + e^{-ip_3} & -2t \cos q_1 & 2t(\cos q_2 - i \sin q_3) \\ e^{ip_2} + e^{ip_3} & -e^{ip_1} & e^{-ip_2} - e^{-ip_3} & -e^{-ip_1} & 2t(\cos q_2 + i \sin q_3) & 2t \cos q_1 \end{pmatrix}. \quad (\text{B1})$$

At $t = J_2/J_1 = 0$, when we only have a small NN triangular lattice, the spectrum has a simple form. It becomes a spectrum of three Dirac pairs, having zeros at different points.

$$E_{\tau, \mathbf{k}} = \pm \left[3 + \cos \left[2p_1 + \frac{2\pi}{3}(\tau - 2) \right] + \cos \left[2p_2 + \frac{2\pi}{3}(\tau - 2) \right] - \cos \left[2p_3 + \frac{2\pi}{3}(\tau - 2) \right] \right], \quad \tau = 1, 2, 3$$

The terms $2\pi(\tau - 2)/3$ in the arguments of the cosine functions appear due to the relative $2\pi/3$ rotations of three NNN sublattices. The $\propto J_2$ terms in the Hamiltonian (B1) also have zeros at the same points, therefore common Dirac points are P_τ and \bar{P}_τ , $\tau = 1, 2, 3$. The chirality of point \bar{P}_τ , $\tau = 1, 2, 3$, is opposite to that of P_τ . The linear expansion of the spectrum around Dirac points gives anisotropic dispersion $E_{\tau, \mathbf{k}}^0 = \left[\sum_\mu (1 + 3t^2)p_\mu^2 - 4tp_\tau q_\tau \right]^{1/2}$.

Appendix C: Self-consistency equations

1. Chern-Simons superconductor description of the 120° phase

Following the steps outlined in Ref. 30, we obtain the BdG Hamiltonian of the mean-field CS superconductor. In terms of the scalar order parameters $\Delta_{0,\mathbf{k}}$ and $\Delta_{3,\mathbf{k}}$, the self-consistency conditions take the closed form:

$$\Delta_{0\mathbf{k}} = \frac{2\pi e}{3} \sum_{a=\pm, \mathbf{k}'} \sum_{\mu=1}^3 \frac{\Delta_{3\mathbf{k}'}}{\mathbf{k}^2 E_{\mathbf{k}'}^{(a)}} A_{\mathbf{k}-\mathbf{k}'}^{\mu} k_{\mu}, \quad \Delta_{3\mathbf{k}} = \pi e \sum_{a=\pm, \mathbf{k}'} \sum_{\mu=1}^3 \frac{1}{E_{\mathbf{k}'}^{(a)}} \left[u A_{\mathbf{k}-\mathbf{k}'}^{\mu} k'_{\mu} + 2w \mathbf{A}_{\mathbf{k}-\mathbf{k}'} (\mathbf{e}_3 q'_3 + \mathbf{a}_3 p'_3) \right], \quad (\text{C1})$$

where $u = (av_0 - (1+t^2)\Delta_{0\mathbf{k}'})$ and $w = t \left(\frac{2a(1+t^2)}{v_0} - \frac{4t\Delta_{0\mathbf{k}'}}{3} \right) / \sqrt{3}$, with $v_0 = \sqrt{(1+3t^2)^2 - \frac{16}{3}t^2}$. The order parameters, Eq. (C1), define the four-band Bogolyubov spectra, $\pm E_{\tau, \mathbf{k}}^{(a)}$, $a = \pm$, of gapped fermions as

$$E_{\tau, \mathbf{k}}^{(a)} = \left[\sum_{\mu=1}^3 p_{\mu}^2 \left[(1 + \Delta_{0\mathbf{k}}^2)(1 + 3t^2) - 2av_0\Delta_{0\mathbf{k}} \right] - 4t(1 - \Delta_{0\mathbf{k}}^2)p_{\tau}q_{\tau} + \Delta_{3\mathbf{k}}^2 \right]^{1/2}. \quad (\text{C2})$$

At $t = 0$, the self-consistency equations are independent of any continuous parameters (momentum cutoff is defined by the size of the Brillouin zone and is not a model parameter). The existence of the solution within superconducting mean-field approach depends on the interaction strength, and thus on the CS charge, $e = 1, 3, 5 \dots$. Here we have one continuous parameter, t , and the anisotropy parameter g is set to zero. At $t = 0$, the only solution that corresponds to $e = 1$ is the trivial one, where there is no superconducting order. However, if the CS-fermionization is realized with $e = 3$, a nontrivial solution of gap equations emerges for $0 \lesssim t \lesssim 0.089$.

One can see that Eqs. (C1) coincide with the analogous self-consistency relations of the CS superconductor on the honeycomb lattice at $t = 0$, first derived in Ref. 30. This indicates the lattice independent ‘universal’ character of CS superconductivity.

2. Chern-Simons superconductor description of the stripe phase

Here we proceed with the fermionic description of the collinear stripe phase. The corresponding π -flux configuration is shown in Fig. 2d of the main text. The BZ is still the same, but Dirac points now are located at $Q = (\arccos(t), 0)$ and $Q' = (-\arccos(t), 0)$. We see that the parity transformations, $\mathcal{P}_{x/y}$, transform one Dirac point to the other, indicating that the ground state does not support the degeneracy of the 120° ordered state. In the vicinity of these Dirac points the Hamiltonian acquires an especially simple form:

$$H_{\text{str},0}^{(Q)}(\mathbf{k}) = J_1 \varepsilon \sum_{\mathbf{k}} \hat{f}_{\mathbf{k},\alpha}^+ [v_y k_y \sigma_{\alpha\beta}^1 - v_x k_x \sigma_{\alpha\beta}^3] \hat{f}_{\mathbf{k},\beta}, \quad (\text{C3})$$

with $v_x = \sqrt{1-t^2}$, $v_y = \sqrt{\frac{3(1-t)}{8}}(1-2t)(1+t)$, and $H_{\text{str},0}^{(Q')}(\mathbf{k}) = -H_{\text{str},0}^{(Q)}(\mathbf{k})$. The generated interaction vertex, $V_{\mathbf{q}}^{\alpha\alpha',\beta\beta'}$, in this case is similar to the one of the 120° phase given below Eq. (6) of the main text, but with $B_{\mathbf{q}}^1 = -v_y A_{\mathbf{q}}^x$, $B_{\mathbf{q}}^2 = 0$, $B_{\mathbf{q}}^3 = -v_x A_{\mathbf{q}}^y$. As in the case of the 120° ordered state, here we also expect that $\Delta_{\mathbf{k}}^{\alpha\alpha'}$ has a $p \pm ip$ -wave symmetry, and the self-consistency relations are given by Eq. (C1). The Bogolyubov mean-field treatment of the full Hamiltonian, $\mathcal{H}_{\text{str}} = H_{\text{str},0}^{(Q)} + H_{\text{str},0}^{(Q')} + H_{\text{int}}$, gives rise to a quasiparticle spectrum of the form

$$E_{\mathbf{k}}^{(s,a)} = \left[(av_x - v_y \Delta_{0\mathbf{k}})^2 k_x^2 + (av_y - v_x \Delta_{0\mathbf{k}})^2 k_y^2 + \Delta_{3\mathbf{k}}^2 \right]^{1/2}. \quad (\text{C4})$$

Appendix D: Emergence of the Dirac Spin-Liquid

As we see in Fig. (5) of the main text, massless Dirac fermions emerge in the parameter interval $0.089 \lesssim t \lesssim 0.116$. Since the double degeneracy of the 120° configuration of the the XX magnet implies a double degeneracy of the π -flux state of fermions on the triangular lattice, our approach indicates that the emergent Dirac spin-liquid state will also be doubly degenerate.

The low-energy field theory in this regime appears to be quite interesting. To understand its nature, one should integrate out fermionic degrees of freedom. In the interaction Hamiltonian, Eq. (6) of the main text, only small values of momentum q contribute to the formation of the order parameter Δ_{120° . Momenta larger than a certain momentum cutoff, $q \gtrsim \tilde{Q}$, are irrelevant for the low-energy description of this ordered phase. When we approach criticality near

$t \sim 0.089$, the fermion gap Δ_{120° vanishes, and critical fermions with large momenta yield the Maxwell term. Indeed, the fermions do not fill any topological bands (e.g. we do not have a Chern insulator coupled to the gauge field) and integration over them will not result in generation of a Chern-Simons term⁵⁰. We rather have topologically trivial Dirac fermions coupled to the $U(1)$ "probe" field. Quantum fluctuations of fermions define an effective dynamics of the gauge field, which in the leading, one loop approximation yields a 2+1 dimensional Maxwell theory. Thus at $0.116 \gtrsim t \gtrsim 0.089$, one self-consistently obtains $N = 6$ copies of Dirac fermions interacting with the induced $U(1)$ gauge field.

-
- ¹ P. Fazekas and P. W. Anderson, *Phil. Mag.* **30**, 423 (1974).
² L. Balents, *Nature (London)* **464**, 199 (2010).
³ A.Y. Kitaev, *Ann.Phys.* **303**, 2 (2003).
⁴ L. Savary and L. Balents, *Rep. Prog. Phys.* **80**, 016502 (2016).
⁵ M. R. Norman, *Rev. Mod. Phys.* **88**, 041002 (2016).
⁶ X. G. Wen, *Rev. Mod. Phys.* **89**, 041004 (2017).
⁷ Y. Zhou, K. Kanoda, and T.-K. Ng, *Rev. Mod. Phys.* **89**, 025003 (2017).
⁸ J. Knolle and R. Moessner, *Annu. Rev. Condens. Matter Phys.* **10**, 451 (2019).
⁹ C. Broholm, R. J. Cava, S. A. Kivelson, D. G. Nocera, M. R. Norman, T. Senthil, "Quantum Spin Liquids," arXiv:1905.07040
¹⁰ P. W. Anderson, *Mater. Res. Bull.* **8**, 153 (1973).
¹¹ S. Sachdev, *Phys. Rev. B* **45**, 12377 (1992).
¹² R. Moessner and S. L. Sondhi, *Phys. Rev. Lett.* **86**, 1881 (2001).
¹³ R. Moessner and S. L. Sondhi, *Prog. Theor. Phys. Supplement* **145**, 37 (2002).
¹⁴ F. Wang and A. Vishwanath, *Phys. Rev. B* **74**, 174423 (2006).
¹⁵ A. Wietek and A. M. Läuchli, *Phys. Rev. B* **95**, 035141 (2017).
¹⁶ Yao-Dong Li, Yuan-Ming Lu, and Gang Chen, *Phys. Rev. B* **96**, 054445 (2017).
¹⁷ Yao-Dong Li, Yao Shen, Yuesheng Li, Jun Zhao, and Gang Chen, *Phys. Rev. B* **97**, 125105 (2018).
¹⁸ Z.-X. Luo, E. Lake, J.-W. Mei, and O. A. Starykh, *Phys. Rev. Lett.* **120**, 037204 (2018).
¹⁹ Y. Shen, Y.-D. Li, H. Wo, Y. Li, S. Shen, B. Pan, Q. Wang, H. C. Walker, P. Steffens, M. Boehm, Y. Hao, D. L. Quintero-Castro, L. W. Harriger, M. D. Frontzek, L. Hao, S. Meng, Q. Zhang, G. Chen, and J. Zhao, *Nature (London)* **540**, 559 (2016).
²⁰ Yuesheng Li, Devashibhai Adroja, Pabitra K. Biswas, Peter J. Baker, Qian Zhang, Juanjuan Liu, Alexander A. Tsirlin, Philipp Gegenwart, and Qingming Zhang, *Phys. Rev. Lett.* **117**, 097201 (2016).
²¹ J. A. M. Paddison, M. Daum, Z. L. Dun, G. Ehlers, Y. Liu, M. B. Stone, H. D. Zhou, and M. Mourigal, *Nat. Phys.* (2017), doi:10.1038/nphys3971.
²² R. Kaneko, S. Morita, and M. Imada, *J. Phys. Soc. Jpn.* **83**, 093707 (2014).
²³ Y. Iqbal, W. Hu, R. Thomale, D. Poilblanc, and F. Becca, *Phys. Rev. B* **93**, 144411 (2016).
²⁴ J. Iaconis, C. Liu, G. B. Halasz, and L. Balents, *SciPost Phys.* **4**, 003 (2018).
²⁵ Francesco Ferrari and Federico Becca, *Phys. Rev. X* **9**, 031026 (2019).
²⁶ Z. Zhu and S. R. White, *Phys. Rev. B* **92**, 041105 (2015).
²⁷ W.-J. Hu, S.-S. Gong, W. Zhu, and D. N. Sheng, *Phys. Rev. B* **92**, 140403(R) (2015).
²⁸ Z. Zhu, P. A. Maksimov, S. R. White, and A. L. Chernyshev, *Phys. Rev. Lett.* **119**, 157201 (2017).
²⁹ Z. Zhu, P. A. Maksimov, S. R. White, and A. L. Chernyshev, *Phys. Rev. Lett.* **120**, 207203 (2018).
³⁰ T. A. Sedrakyan, V. M. Galitski, and A. Kamenev, *Phys. Rev. B* **95**, 094511 (2017).
³¹ D. H. Lee, J. D. Joannopoulos, J. W. Negele, and D. P. Landau, *Phys. Rev. Lett.* **52**, 433 (1984).
³² S. Miyashita and H. Shiba, *J. Phys. Soc. Jap.* **53**, 1145 (1984).
³³ S. E. Korshunov, *Physics - Uspekhi* **49** (3) 225 - 262 (2006).
³⁴ M. Ye and A. V. Chubukov, *Phys. Rev. B* **95**, 014425 (2017).
³⁵ M. Ye and A. V. Chubukov, *Phys. Rev. B* **97**, 245112 (2018).
³⁶ R. Wang, B. Wang, and T. A. Sedrakyan, *Phys. Rev. B* **98**, 064402 (2018).
³⁷ T. A. Sedrakyan, L. I. Glazman, and A. Kamenev, *Phys. Rev. Lett.* **114**, 037203 (2015).
³⁸ T. A. Sedrakyan, A. Kamenev, and L. I. Glazman, *Phys. Rev. A* **86**, 063639 (2012).
³⁹ T. A. Sedrakyan, L. I. Glazman, and A. Kamenev, *Phys. Rev. B* **89**, 201112(R) (2014).
⁴⁰ S. Maiti and T. Sedrakyan, *Phys. Rev. B* **99**, 174418 (2019).
⁴¹ J. Villain, *J. Phys. France* **38**, 4 (1977) 385-39.
⁴² H. Kawamura, *Phys. Rev. B* **38**, 4916 (1988).
⁴³ Michael Hermele, T. Senthil, Matthew P. A. Fisher, Patrick A. Lee, Naoto Nagaosa, and Xiao-Gang Wen, *Phys. Rev. B* **70**, 214437 (2004).
⁴⁴ Xiao-Gang Wen, *Phys. Rev. B* **65**, 165113 (2002).
⁴⁵ S. Bieri, C. Lhuillier, and L. Messio, *Phys. Rev. B* **93**, 094437 (2016).
⁴⁶ S.V. Maleyev, *Physica B* **345**, 119-123 (2004).
⁴⁷ V. Simonet, M. Loire, and R. Ballou, *Eur. Phys. J. Special Topics* **213**, 5-36 (2012).
⁴⁸ E. Ressouche, "Polarized neutron diffraction," *Collection SFN* **13**, 02002 (2014).
⁴⁹ D. J. Thouless, M. Kohmoto, M. P. Nightingale, and M. P. M. den Nijs, *Phys. Rev. Lett.*, **49**, 405 (1982).
⁵⁰ G. W. Semenoff, *Phys. Rev. Lett.* **53**, 2449 (1984).